NUMERICAL PROCEDURE FOR THE COMPUTATION OF FLUID FLOW WITH ARBITRARY STRESS-STRAIN RELATIONSHIPS

Paulo J. Oliveira
Departamento de Engenharia Electromecânica, Universidade da Beira Interior, 6200 Covilhã, Portugal

Fernando T. Pinho
Centro de Estudos de Fenómenos de Transporte, DEMEGI, Faculdade de Engenharia, Universidade do Porto, 4099 Porto Codex, Portugal

A finite-volume method is presented that allows for general stress-strain constitutive equations to be incorporated into a standard momentum–pressure-correction procedure. The method is sequential and segregated in nature, the various equations for mass and momentum conservation and for the evolution of the stress tensor are solved following a predefined order, and one of its features is the use of nonstaggered, and generally nonorthogonal, computational meshes. Two types of constitutive equations are used to test the method: the standard explicit and algebraic Newtonian model, and one of the simplest implicit differential equations, the upper-convected Maxwell model. In spite of its apparent simplicity, this latter model is known to pose the most severe numerical difficulties. However, the results in this article show the method to be effective in solving the equations for the flow of Newtonian and viscoelastic fluids through abrupt planar contractions with an area reduction of 4 to 1, one typical benchmark problem. The results are compared with available data and with solutions from a standard and validated code, and good agreement and consistency is found. A new formulation to evaluate stresses at cell faces is presented and shown to lead to improved results.

1. INTRODUCTION

Most procedures to calculate fluid flow are based on Newtonian constitutive stress-strain relationships that are implicitly embedded into the flow equations, resulting in the usual Navier-Stokes equations. However, very often real fluids exhibit non-Newtonian viscoelastic behavior, and in such cases it is neither advantageous nor always possible to find an explicit relation between the stress tensor and velocity gradient components to substitute into the momentum equations. As a consequence, it is useful to develop numerical procedures adequate for general stress tensors, which are often related with the flow kinematics in a complex and implicit manner via additional differential equations, thus separating the stress calculation from the solution of the momentum equations. The development of such a method is the scope of the present article. The stress-strain relationships to

Address correspondence to Dr. P. J. Oliveira, Universidade da Beira Interior, Departamento de Eng[a] Electromecânica, 6200 Covilhã, Portugal. E-mail: pjpo@ubi.pt

NOMENCLATURE

a_P, a_F	coefficients in the discretized equations	δ_{ij}	identity tensor	
b_{li}	coefficients in the discretized stress equations	$\delta x, \delta y$	cell sizes (normalized as $\delta x/H$)	
		δt	time step	
B, B_{li}	area, i component of area of a cell surface aligned with direction ξ_l	$[\Delta u]_l$	difference between u values along direction l	
De	Deborah number (= $\lambda U/H$)	λ	relaxation time	
f_x, f_y	expansion/contraction factors to distribute cell spacing	μ	viscosity coefficient	
		ν	cell volume	
F_f	mass flow rate across cell face f	ρ	density	
H	half-width of downstream channel	ξ_l	general coordinates	
L_1, L_2	lengths of upstream and downstream channels	τ_{ij}	Cartesian components of the extra stress tensor	
N_1	primary normal-stress difference	Ψ	stream function value	
$p, \mathbf{P}$	pressure, normalized pressure (= $p/(\mu U/H)$)			

Subscripts and Superscripts

Re	Reynolds number (= $\rho U H/\mu$)	i, j, k	Cartesian components (from 1 to 3)
S	source term in the discretized equations	l, m	directions along general coordinates (from 1 to 3)
t	time	P, F	generic control volume and neighbor (F from 1 to 6)
T_{ij}	normalized stress components (= $\tau_{ij}/(\mu U/H)$)	f	cell face between cells P and F (varies from 1 to 6)
$u_i, (u, v)$	Cartesian velocity components (streamwise and cross-stream components)	$n, n+1$	denotes previous and present time level, respectively
U	average velocity in downstream channel	$\tilde{\ }$	special cell-face interpolation
$x_i (x, y)$	Cartesian coordinates (streamwise and cross-stream)	$\overline{\ }$	linear interpolation
		$'$	divided by central coefficient a_P
x_R	recirculation length	$*$	intermediate values (calculated implicitly)

be considered will either follow the Newtonian viscosity law, but in this case with the stress components evaluated from independent equations and then incorporated into the stress-divergence term of the momentum equations, or are given by a linear differential equation for the evolution in time of the stress tensor. Future work will consider the case of quasi-linear and nonlinear stress-strain relations.

The developed numerical procedure is of the finite-volume type along the lines exposed by Patankar [1], but incorporating modern techniques such as the use of nonstaggered and nonorthogonal meshes which allows for greater versatility in terms of flow geometry [2, 3]. The important contribution that made possible the widespread use of the nonstaggered mesh arrangement was the novel interpolation scheme of Rhie and Chow [4] for determining velocity values at cell faces, and a similar philosophy has been recently advanced by Oliveira et al. [5] for the problem of determining stress values at cell faces. We shall use here an improvement of this latter method to interpolate the stress components required in the stress-divergence term of the linear momentum equation. The numerical procedure is then applied to a typical problem often used as a test case in the non-Newtonian community [6–10]: the flow of both Newtonian and viscoelastic fluids obeying the

upper-convected Maxwell model (UCM) through a 4-to-1 planar contraction. This particularly simple geometry does not require the nonorthogonal capability of the procedure, a matter left for future investigation. It poses, however, severe numerical difficulties, especially for the UCM fluid [10, 11], because of unbounded stresses at the reentrant corner with a very intense localized growth rate for all stress components; furthermore, for this fluid model the resulting flow features are not yet fully understood (see reviews in [11] and [12]).

2. GOVERNING EQUATIONS AND CONSTITUTIVE MODELS

The basic equations to be solved are those expressing conservation of mass,

$$\frac{\partial \rho u_j}{\partial x_j} = 0 \tag{1}$$

and of linear momentum,

$$\frac{\partial \rho u_i}{\partial t} + \frac{\partial \rho u_j u_i}{\partial x_j} = -\frac{\partial p}{\partial x_i} + \frac{\partial \tau_{ij}}{\partial x_j} \tag{2}$$

In these equations u_i is the velocity component along the Cartesian axis x_i, ρ is the fluid density, and the total Eulerian stress tensor σ_{ij} has been decomposed into an isotropic pressure term plus an extra stress tensor τ_{ij}, as $\sigma_{ij} = -p\delta_{ij} + \tau_{ij}$, where δ_{ij} is the identity tensor. Here we will be concerned with incompressible and steady flow, and the main dependent variables to be solved for are the velocity components, the pressure, and the stress components. The velocity components result from the momentum equation (2), for incompressible flow the pressure is an arbitrary field required to constrain the velocity field so that it conforms to equation (1), and the stress components must be given by a rheological constitutive equation.

In general, the equation for the stress tensor τ_{ij} is of the hyperbolic type [13] and is derived either from continuum mechanics or from kinetic theory [14], where force balances acting on simplified models of molecular behavior are utilized. The precise form of these equations varies according to the fluid considered, but must respect some general rules such as objectivity, realizability, etc., and must also provide physically realistic responses and preferably be supported by kinetic theory arguments. In this article, two constitutive models are considered. First, and in order to compare the present method with standard procedures, we consider the well-known Newtonian model given by the algebraic explicit stress-strain relationship,

$$\tau_{ij} = \mu \left(\frac{\partial u_i}{\partial x_j} + \frac{\partial u_j}{\partial x_i} \right) - \frac{2}{3} \mu \frac{\partial u_k}{\partial x_k} \delta_{ij} \tag{3}$$

where μ is the constant dynamic viscosity of the fluid, and the velocity divergence ($\text{div } u \equiv \partial u_k / \partial x_k$) in the last term vanishes for incompressible flows but is

nevertheless retained because it is not exactly zero in the numerical approximation when the nonstaggered mesh arrangement is utilized. Besides, inclusion of this term leads to more accurate results, as will be shown in Section 4.

The second constitutive equation considered for the extra stress components τ_{ij} is the upper-convected Maxwell model (UCM) [13],

$$\tau_{ij} + \lambda\left(\frac{\partial \tau_{ij}}{\partial t} + \frac{\partial u_k \tau_{ij}}{\partial x_k}\right) = \mu\left(\frac{\partial u_i}{\partial x_j} + \frac{\partial u_j}{\partial x_i} - \frac{2}{3}\frac{\partial u_k}{\partial x_k}\delta_{ij}\right)$$
$$+ \lambda\left(\tau_{ik}\frac{\partial u_j}{\partial x_k} + \tau_{jk}\frac{\partial u_i}{\partial x_k}\right) \tag{4}$$

where μ can still be seen as a constant viscosity coefficient and λ is another parameter of the model with the dimensions of time and commonly called the relaxation time of the fluid. Equation (4) is one of the simplest models to represent viscoelastic fluid behavior, and it is noted that the Newtonian model is obtained as a special case of the UCM model when λ is set to zero. However, in the general case of $\lambda \neq 0$, the UCM equations introduce considerable complication into the problem of determining the motion of a fluid: six new implicit differential equations on the stresses have to be solved in conjunction with the momentum and mass conservation equations. Furthermore, although Eq. (4) is linear on the stresses τ_{ij}, when coupled with Eq. (2), implicit nonlinearities will arise through the terms with velocity gradients.

3. NUMERICAL METHOD

The differential equations are integrated over control volumes in general body-fitted computational meshes (ξ_l) with the help of standard discretization procedures [1, 2]. The dependent variables are the three Cartesian velocity components, the pressure, and the six Cartesian stress components; all these variables are stored at the center of the control volumes, as implied by the nonstaggered mesh arrangement adopted here. Special procedures are thus required to avoid pressure–velocity decoupling [4] and stress–velocity decoupling [5]. Details of the discretization procedure can be found in the latter reference and here, for the sake of conciseness, only the constitutive equation will be treated with more detail.

Discretization of the continuity Eq. (1) gives

$$\sum_f^6 F_f = 0 \qquad \left[\text{with } F_f = \sum_j \left(\rho B_{fj}\tilde{u}_j\right)_f\right] \tag{5}$$

expressing mass conservation: the sum of the outgoing mass flow rates (F_f) over the six faces delimiting any given cell must vanish. The tilde over the velocity is used to denote a special Rhie-and-Chow type of interpolation; the precise form is as given in [15]. Here, and in the following, the i component of the area of any cell surface oriented along direction ξ_l is denoted B_{li}; if this surface coincides with an actual cell face with direction ξ_f, then we write B_{fi} as the i component of that cell face area (the scalar area is $B_f = (\sum_j B_{fj}B_{fj})^{1/2}$).

After discretization over any cell P, the momentum equation can be written under the standard linearized form:

$$a_P(u_i)_P = \sum_F^6 a_F(u_i)_F + S_{u_i} \tag{6}$$

where the coefficients a_F are made up of convective and diffusive contributions, whose precise form depends on the differencing schemes adopted, and the central coefficient is

$$a_P = \frac{\rho v}{\delta t} + a_0 \qquad \text{with } a_0 = \sum a_F \tag{7}$$

the sum being again over the six cell neighbors (F) surrounding the cell P under consideration. Here δt is the time step used in the time-marching computations. The source term in Eq. (6) results from all contributions in the momentum equation that have not been included into the coefficients and, from inspection of Eq. (2), these are

$$S_{u_i} = S_{u_{i-\text{pres}}} + S_{u_{i-\text{stress}}} + S_{u_{i-\delta t}} + S_{u_{i-\text{HOS}}} + S_{u_{i-\text{diff}}} \tag{8}$$

for the pressure gradient, the stress divergence, the inertia term, a possible term arising from use of a high-order differencing scheme (HOS) for convection, and an added diffusion term that cancels exactly the diffusion contribution in the coefficients, since there is no explicit diffusion in the original equation [Eq. (2)].

The discretized stress equation (4) can be cast into a form similar to Eq. (6) as

$$a_P^\tau(\tau_{ij})_P = \sum_F^6 a_F^\tau(\tau_{ij})_F + S_{\tau_{ij}} \tag{9}$$

with the central coefficient now given by

$$a_P^\tau = v + \frac{\lambda v}{\delta t} + a_0^\tau \tag{10}$$

and the other coefficients composed only of convective fluxes due to the absence of diffusion in the constitutive equation (4). It is straightforward to arrive at the source term in the stress equation after transforming the Cartesian derivatives in Eq. (4) into derivatives with respect to the general coordinates, by making use of the rule $\partial / \partial x_i = J^{-1} \beta_{li} \, \partial / \partial \xi_l$, and realizing that in the discretized equations the Jacobian J becomes a cell volume v and the metric coefficients β_{li} become area components B_{li} [16]; that source term can then be written as

$$S_{\tau_{ij}} = \sum_l^3 \left(b_{li}[\Delta u_j]_l + b_{lj}[\Delta u_i]_l - \frac{2}{3} \left(\sum_k \mu B_{lk}[\Delta u_k]_l \right) \delta_{ij} \right)_P$$
$$+ \frac{\lambda v}{\delta t}(\tau_{ij}^n)_P + S_{\tau_{ij-\text{HOS}}} \tag{11}$$

where the term multiplied by $\frac{2}{3}$ results from keeping the div u term in the Newtonian part of the constitutive equation and the b coefficients are given by

$$b_{li} = \mu B_{li} + \lambda \sum_k B_{lk} \tau_{ik} \tag{12}$$

One key feature in the numerical procedure is the determination of the stress components at cell faces $(\tilde{\tau}_{ij})$ required for the divergence term in the momentum equation, that is,

$$S_{u_{i-\text{stress}}} = \sum_f^6 \left(\sum_j B_{fj} \tilde{\tau}_{ij} \right)_f \tag{13}$$

In order to avoid stress-velocity decoupling and along the lines of the procedure given by [5], the face stresses are defined as

$$(\tilde{\tau}_{ij})_f \equiv \overline{\sum_F a_F^\tau (\tau_{ij})_F} + \sum_{l \ne f} \overline{\left(b_{li}'[\Delta u_j]_l + b_{lj}'[\Delta u_i]_l - \frac{2}{3} \sum_k \mu B_{lk}'[\Delta u_k]_l \delta_{ij} \right)_f}$$
$$+ \tilde{b}_{fi}'[\Delta u_j]_f + \tilde{b}_{fj}'[\Delta u_i]_f - \frac{2}{3} \sum_k \overline{\mu} \tilde{B}_{fk}'[\Delta u_k]_f \delta_{ij} + \overline{\left(\frac{\lambda v}{\delta t} \right)' (\tau_{ij}^n)_P} + S_{\tau_{ij} - \text{HOS}} \tag{14}$$

where the overbar here denotes linear interpolation at the cell face position, and the prime denotes division by the central coefficient a_P^τ. It is simpler to use the following expression, obtained after dividing Eq. (9) by the central coefficient, applying linear averaging to it, and subtracting the resulting equation from Eq. (14):

$$(\tilde{\tau}_{ij})_f = (\overline{\tau_{ij}})_f - \overline{\left(b_{fi}'[\Delta u_j]_f + b_{fj}'[\Delta u_i]_f - \frac{2}{3} \sum_k \mu B_{fk}'[\Delta u_k]_f \delta_{ij} \right)}$$
$$+ \left(\tilde{b}_{fi}'[\Delta u_j]_f + \tilde{b}_{fj}'[\Delta u_i]_f - \frac{2}{3} \sum_k \overline{\mu} \tilde{B}_{fk}'[\Delta u_k]_f \delta_{ij} \right) \tag{15}$$

with

$$\tilde{b}_{fi}' \equiv \frac{\overline{\left(\overline{\mu} B_{fi} + \overline{\lambda} \sum_j B_{fj} \overline{\tau_{ij}} \right)_f}}{v_f (a_P^\tau / v_P)} \quad \text{and} \quad \tilde{B}_{fi}' \equiv \frac{B_{fi}}{v_f (a_P^\tau / v_P)} \tag{16}$$

Expression (15) is essential to avoid the problem of stress–velocity decoupling and is only slightly different from that proposed in our previous work [5], yet it improves the results, yielding better stress interpolation when the mesh spacing changes abruptly, as will be shown below.

Solution Procedure

The sets of discretized equations are solved in a sequential manner following a pseudo-time-marching approach described below, where new or intermediate values are denoted with an asterisk, and values from the previous time step with index n.

1. Obtain cell-centered stresses (τ_{ij}^*) from the implicit equation [Eq. (9)],

$$a_P^\tau (\tau_{ij})_P^* = \sum_F^6 a_F^\tau (\tau_{ij})_F^* + \left(S_{\tau_{ij}} \right)^n \qquad (17)$$

   and store the central coefficient a_P^τ.
2. Compute cell face stresses $(\tilde{\tau}_{ij})$ from Eq. (15), based on newly obtained stresses τ_{ij}^*, the stored central coefficient a_P^τ, and velocity gradients at the previous time step.
3. Solve for the Cartesian velocity components at cell centers, u_i^*, from the discretized momentum conservation equation [Eq. (6)],

$$a_P (u_i)_P^* = \sum_F^6 a_F (u_i)_F^* + \left(S_{u_i} \right)^n \qquad (18)$$

4. Obtain cell face velocities (see [15]) and form the corresponding mass flow rates (Eq. 5),

$$F_f^* = \sum_j \left(\rho B_{fj} \tilde{u}_j^* \right)_f$$

5. Solve the pressure-correction equation (following the SIMPLEC algorithm of [17]; see [15] for the time-marching version) and correct the pressure field, p^*, the velocity field, u^{**}, and the mass flow rates, F_f^{**}, which will now satisfy the continuity constraint.
6. Check for convergence to a steady state, when the norm of the residuals of all equations has fallen below a prescribed tolerance (10^{-4}); otherwise, take the variables as pertaining to a new time level $(n+1)$ and go back to step 1.

Implicit solution of the linear sets of equations in steps 1, 3, and 5 is carried out by application of standard preconditioned conjugate gradient methods [16].

4. RESULTS

The numerical method described above was implemented into a computational code that we shall denote as the "stress" code, and was then applied to a typical problem: the flow of Newtonian and UCM fluids through a planar contraction with a cross-sectional area ratio of 4 to 1. This particular flow has been often used as a test case in the non-Newtonian community—see, for example, Marchal

and Crochet [6], Webster and co-workers [10, 11], Xue et al. [12], to name only a few of the relevant works. The flow is completely described by two nondimensional parameters, the Reynolds and Deborah numbers. The former is defined here with the average velocity U in the downstream channel of half-width H, $\mathrm{Re} = \rho U H / \mu$, and the latter gives an indication of the elasticity of the UCM fluid, $\mathrm{De} = \lambda U / H$.

Results are first presented for the Newtonian case, $\mathrm{De} = 0$, allowing comparison between the present "stress" code and a "standard" Navier-Stokes solver which has been used in previous work and is by now sufficiently validated (e.g., [15, 16, 18]). This standard code solves the momentum and continuity equations in collocated meshes and is essentially similar to that developed by Perić [2]. Agreement between the results of the two codes will give an indication of the correct implementation of the method developed to handle general stress equations.

Then, the flow of the UCM fluid with increasing degree of elasticity will be considered, mainly for $\mathrm{Re} = 1$. Here we will concentrate on the streamline patterns and on the stress fields, which show interesting phenomena that are not present in the Newtonian case. Where possible, comparisons are made between our predictions and others from the literature.

Newtonian Fluid

The contraction geometry has been mapped with three successively refined computational meshes, of which Figure 1 shows a zoomed portion of the finest (mesh 3). The mesh is orthogonal but nonuniform, with increased concentration of cells in the area of the contraction, especially around the reentrant corner where the stress gradients are expected to be high. For the mesh of Figure 1, the minimum nondimensional cell size is 0.01 in both the x and y directions $[(\delta x / H)_{\min}$ and $(\delta y / H)_{\min}]$; this value is doubled for the medium mesh 2 and doubled again for the coarse mesh 1. In each mesh the cell size varies following a geometric progression at constant ratio $(f_x \equiv \delta x_{i+1} / \delta x_i)$ inside each subblock used to generate the overall mesh. The f_x and f_y were carefully chosen to guarantee a smooth cell-size variation at boundaries between the patched subblocks. In order to go from mesh 1 (the coarsest) to mesh 2 (the medium), and from mesh 2 to mesh 3 (the finest), the number of cells along the x and y directions inside each subblock was doubled and the corresponding expansion / contraction ratios $(f_x$ and $f_y)$ were root-squared. With this procedure a consistent refinement is achieved in these nonuniform meshes (see [19]), with all mesh spacings being approximately halved at each step and enabling error estimation through Richardson's extrapolation to the limit. Other details of the meshes are given in Table 1, where NC is the total number of cells and where the inlet and outlet channel lengths were taken as $L_1 = 20 H$ and $L_2 = 50 H$, respectively. These lengths were found sufficient to achieve fully developed conditions at the outlet in both the Newtonian and in all the elastic flow cases.

The results to be given were obtained with the finer mesh unless stated otherwise. The effect of mesh refinement can be assessed from the values for the length of the recirculation zone in the salient corner (x_R) and the amount of flow in the eddy scaled with the inlet flow rate (Ψ_R) given in Table 2. They were obtained using both the central differencing scheme (CDS) and the upwind scheme
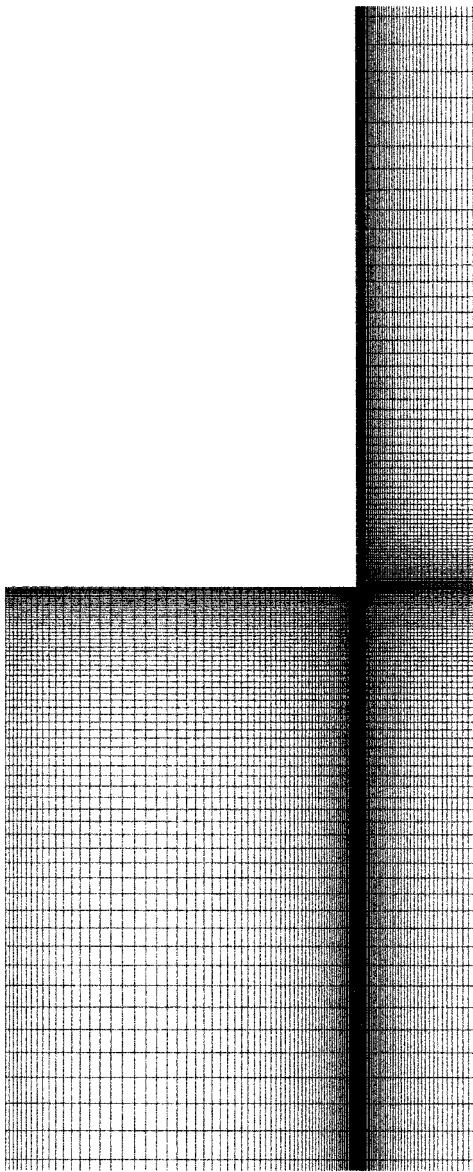
Figure 1. Zoomed view of the finer mesh (mesh 3).

Table 1. Mesh characteristics

Mesh	NC	$(\delta x/H)_{min}$	f_x	f_y
Mesh 1	942	0.04	1.2179	0.8475
Mesh 2	3598	0.02	1.1036	0.9206
Mesh 3	14258	0.01	1.0505	0.9595

Note: f_x and f_y are for the subblock in the downstream channel.

Table 2. Eddy characteristics with mesh refinement

Mesh	$\Psi_R \times 10^{-4}$	x_R/H	$(N_{1max})_{CL}$	$\Psi_R \times 10^{-4}$ (UDS)	x_R/H (UDS)
Mesh 1	4.83751	1.1838	2.2672	5.29766	1.2073
Mesh 2	4.39882	1.2020	2.2912	4.60744	1.2141
Mesh 3	4.37856	1.2072	2.2896	4.48108	1.2134
Limit	4.37975	1.2090			

(UDS) for the convective terms in the momentum equations. There is little difference between the results of the two schemes (especially for x_R), an expected outcome for this low-Reynolds-number flow (recall that Re = 1 and so the local cell Reynolds number is much lower still), but the CDS being ideally second-order accurate enables better Richardson extrapolation.

Based on the values in Table 2, the error estimate for the simulation in the fine mesh is 0.15% and the medium mesh is able to give results for eddy size and intensity to within 1.0%. Richardson's theory gives the order of the numerical approximation as $p = \ln[(x_{R2} - x_{R1})/(x_{R3} - x_{R2})]/\ln(2) = 1.81$, based on the x_R values in the three meshes, in good agreement with the theoretical value of 2 for the central differencing scheme. Mesh 2 and mesh 3 also show good superposition of local quantities, as exemplified in the profile of the first normal stress difference $[N_1 = T_{xx} - T_{yy},$ where T_{ij} are normalized stresses, $T_{ij} = \tau_{ij}/(\mu U/H)]$ along the centerline ($y = 0$), given in Figure 2. The maxima of these profiles are given in Table 2, useful data for benchmarking. Similar convergence with mesh refinement has been found for other variables, such as velocity and stress components, but this comparison is not shown here for conciseness. For the viscoelastic fluid obeying the UCM constitutive equation there is a tendency for finer meshes to be required as the Deborah number is increased, due to the resulting steeper stress gradients. However, at De = 2 the results with mesh 2 and mesh 3 are still not too different, as shown in Figure 2, although accuracy to the same level attained by the Newtonian runs may require finer meshes.

The results for Newtonian fluids obtained with the "stress" code are in excellent agreement with those obtained with the standard code, which yields $\Psi_R = 4.3869 \times 10^{-4}$ and $x_R/H = 1.2076$ for mesh 3. It has also been checked that profiles of local variables at various locations agreed very closely, and consequently we may conclude that the implementation of the stress method has been done correctly. In terms of convergence rate, Figure 3 compares the history of the residuals for the two codes and for the combination of parameters Re = 1, De = 0,
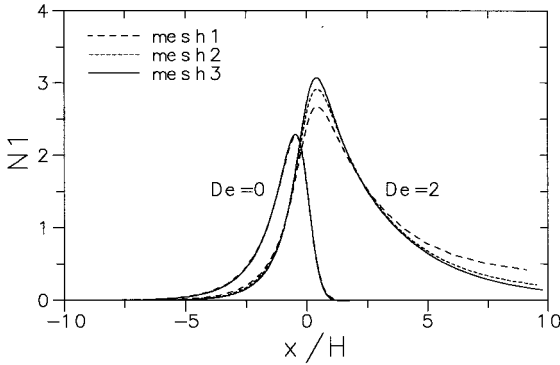
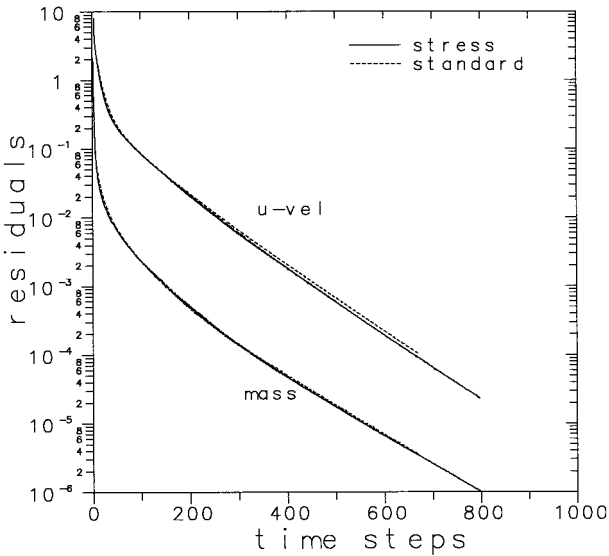**Figure 2.** Effect of mesh refinement on the primary normal stress difference along the centerline (De = 0 and 2).

Figure 3. Decay of the norm of the residuals of the u momentum and continuity equations for the "stress" and "standard" procedures.

mesh 2, $\delta t/(H/U) = 0.01$, with a converged solution being assumed when the normalized residuals of all equations fell below a tolerance of 10^{-4}. These residuals are defined as the l_1 norm of the algebraic equations to be solved, with all terms shifted to one side of the equal sign, and should essentially tend to zero as the solution is approached. Figure 3 shows that the new method follows an identical convergence path to the standard one, and the number of time steps to the solution is only slightly higher (798 compared with 674), because the residuals of the stress equations (not shown in Figure 3) are now also considered in the

stopping criterion and tend to lag behind those for the momentum and mass conservation equations. Still, for an identical stopping criterion, the CPU required by the new method when applied to a Newtonian fluid is only 18% larger than that of the standard procedure, a reasonable computing time overhead to pay for the added advantage of choosing any general constitutive relation. Naturally, the use of a different constitutive equation will require additional computer time.

It is interesting and relevant at this stage to corroborate the point made in Section 2, that inclusion of the $-\frac{2}{3}\,\mathrm{div}\,u$ term in the stress equation for the Newtonian fluid tends to give more accurate results and is also better at reducing the computing time. Figure 4a compares the normalized pressure variation $P \equiv p/(\mu U/H)$ at the entrance to the smaller channel, just downstream of the contraction plane, with and without the div u-term and using the medium-sized mesh. When the div u term is not included to force a traceless deviatoric stress tensor, there are some perturbations in the pressure profile near the wall (at $y/H \simeq 1$). Similar unphysical perturbations are observed in the lateral component of the velocity v/U (Figure 4b) and the normal stress component T_{yy} (Figure 4c), but they are suppressed when the div u term is included in the stress tensor. In general, not including this term leads to higher maximum levels of pressure and stress components [e.g., $(T_{xx})_{\max}$ increases from -5.1 to -7.4], which typically occur close to the reentrant corner where the high gradients are localized, and the computing time increases by 30% and 15% in the two tested cases (Re $= 0.01$ and 1, respectively).

Viscoelastic Fluid

We turn now to the more complicated case of the implicit differential UCM constitutive equation [Eq. (4)], which was solved with the procedure outlined in Section 3. Since the stress contribution to the momentum balance [the div τ term given by Eq. (13)] is treated explicitly in the numerical method, so that it lags in time as the solution is reached through a sequential treatment of the various equations, it is expected that convergence to a steady state will be slower than for the Newtonian fluid. This is indeed the case as shown in Figure 5, which gives the history of the residuals for the slowest variable, for various runs with increasing values of De. The runs for the Newtonian fluid (De $= 0$) and for De $= 1$ have been started from an initial condition of uniform velocities and vanishing stresses and pressure everywhere; the other runs have been restarted from the corresponding solution at lower Deborah number. This procedure is convenient to reduce computer time but was not found necessary to guarantee convergence. All runs in Figure 5 used the same time step ($\delta t = 10^{-2} H/U$) in spite of increased elasticity, an indication of the robustness of the present numerical method. The convergence rate, proportional to the inclination of the curves, is reduced as De increases, and so computations at high De will require more time steps for a steady solution to be reached. This situation is common to all methods reported in the non-Newtonian literature, most of them of the finite-element type [6, 8–11], and with the drawback that those methods often could only obtain solutions at very low Deborah numbers (e.g., Yoo and Na [7], De $<$ 1.04; Carew et al. [8], De $\leqslant$ 2; Sato and Richardson [9], De $\leqslant$ 2). Marchal and Crochet [6] could attain De $= 6$, but with very coarse meshes.
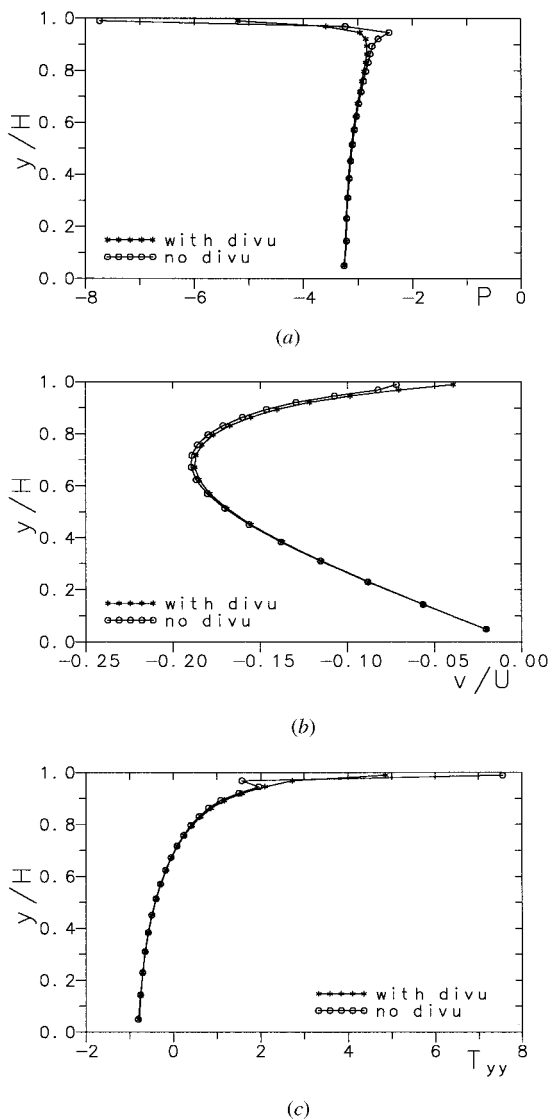
Figure 4. Effect of including the div u term in the constitutive equation: transverse profiles at $x = 0.01 H$ of (a) normalized pressure, (b) v/U, and (c) normal stress T_{yy}.

A comparison of some of the results of the literature and those of the present stress method is carried out in Table 3. The extension of the recirculating zone predicted by [9], utilizing meshes with a minimum spacing of 0.025 and 0.05, compared well with the present predictions, and so did those of [11] for the low-De range. For the high-De number range, however, these latter authors used a mesh that was too coarse to yield adequate predictions (minimum mesh spacing of 0.14),
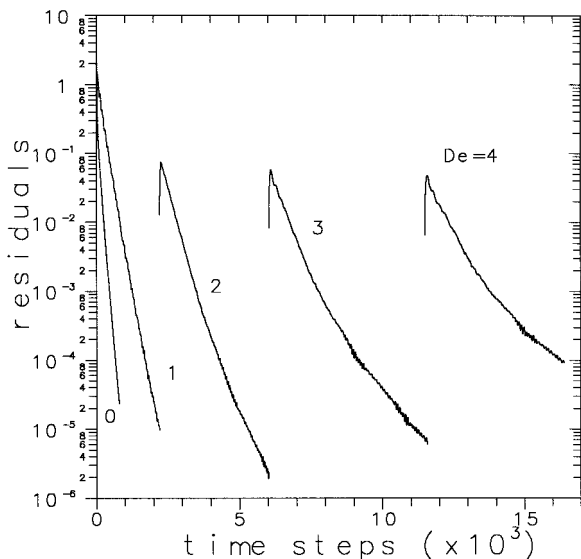
Figure 5. Convergence history for the Newtonian (De = 0) and various UCM fluid flows.

Table 3. Values of x_R/H: comparison with other calculations

De	Sato[a] [9], Re = 1	Ours, Re = 1	Matallah[a] [11], Re = 0.5	Ours[b] Re = 0.5
0	1.145	1.213	1.318	1.341
1	1.000	0.988	1.114	1.189
2	0.927	0.833	1.0	1.175
3	—	0.784	1.0	1.319
4	—	0.851	1.0	1.550
5	—	1.081	—	1.784
6	—	1.339	—	—
8	—	1.755	—	—

[a] Oldroyd-B model.
[b] With mesh 2.

and that may explain the fact that their predictions of x_R tended to a constant value for De $\geqslant$ 2.

Some of the potential of the present method for the study of viscoelastic fluid flow is illustrated by Figure 6, which shows the streamline patterns for increasing De (from 0 to 8) at constant Re = 1, and by Figures 7 and 8, which show some of the corresponding contour plots of the nondimensional normal-stress difference (N_1) and shear stress (T_{xy}) fields, respectively. Careful analysis of these figures and other data from the solution fields, a matter outside the scope of the present article, may explain some of the peculiar features observed in experiments with viscoelastic fluids. The streamline patterns in Figure 6 show the appearance of a lip vortex at De $\approx$ 1 and its growth at De $\approx$ 2–3, fingering of the corner vortex toward
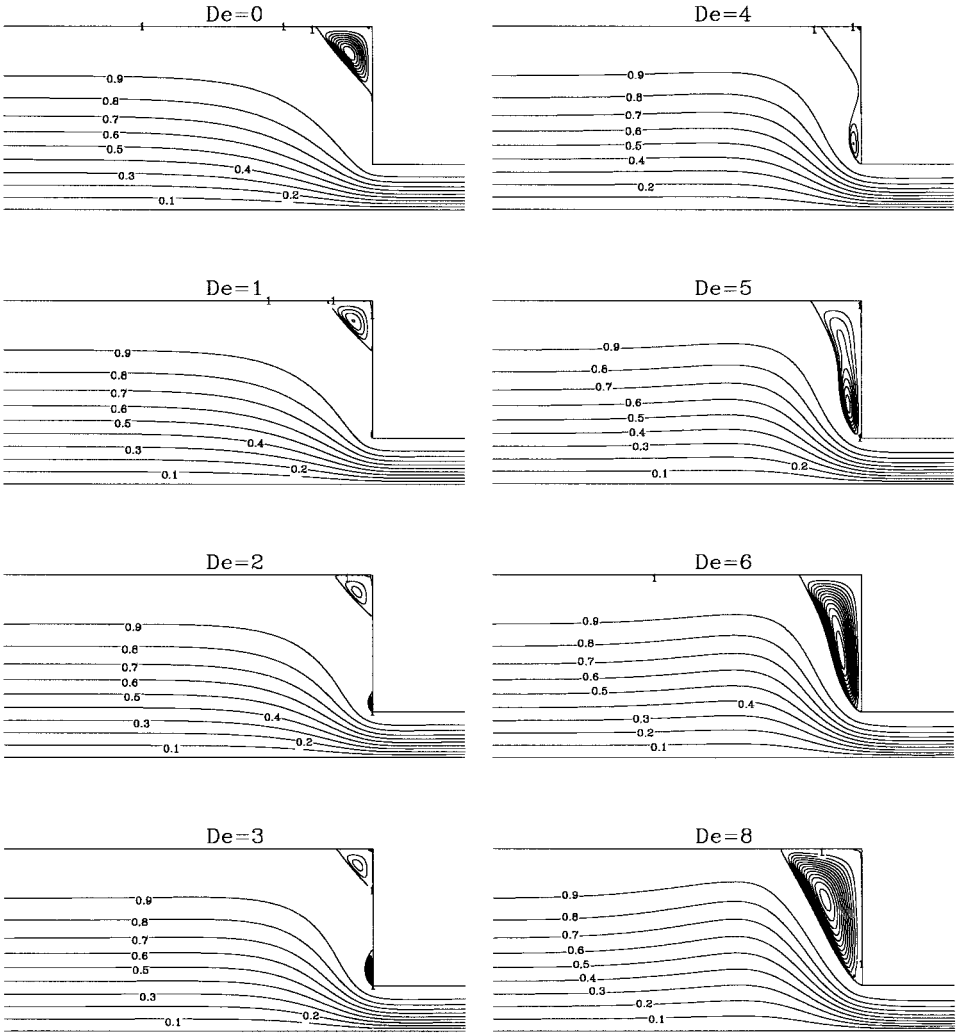
Figure 6. Streamline patterns of UCM fluids for increasing Deborah numbers, at constant Re = 1. (Iso-levels in the eddies are equally spaced, with $\delta\Psi \times 10^3 = 0.05$ for De = 0–3; 0.5 for De = 4–6; and 1.0 for De = 8)

the lip vortex at De $\leqslant$ 4, the eventual merging of the two vortices at De $\simeq$ 4–5, and the subsequent growth of the single remaining vortex. The flow patterns at low De are in good agreement with the recent simulations for an Oldroyd-B fluid of Matallah et al. [11] (mainly so for De = 1 to 3), which also show the onset of the lip vortex that has been quite elusive in previous works (e.g., Sato and Richardson [9]; see also review in [11]). We may also add that the flow features seen in Figure 6 are not just a peculiar effect resulting from the theoretical UCM model and absent from the reality; in fact, similar vortex-related phenomena have been observed experimentally in flow visualizations by Walters (in planar contractions) and Boger
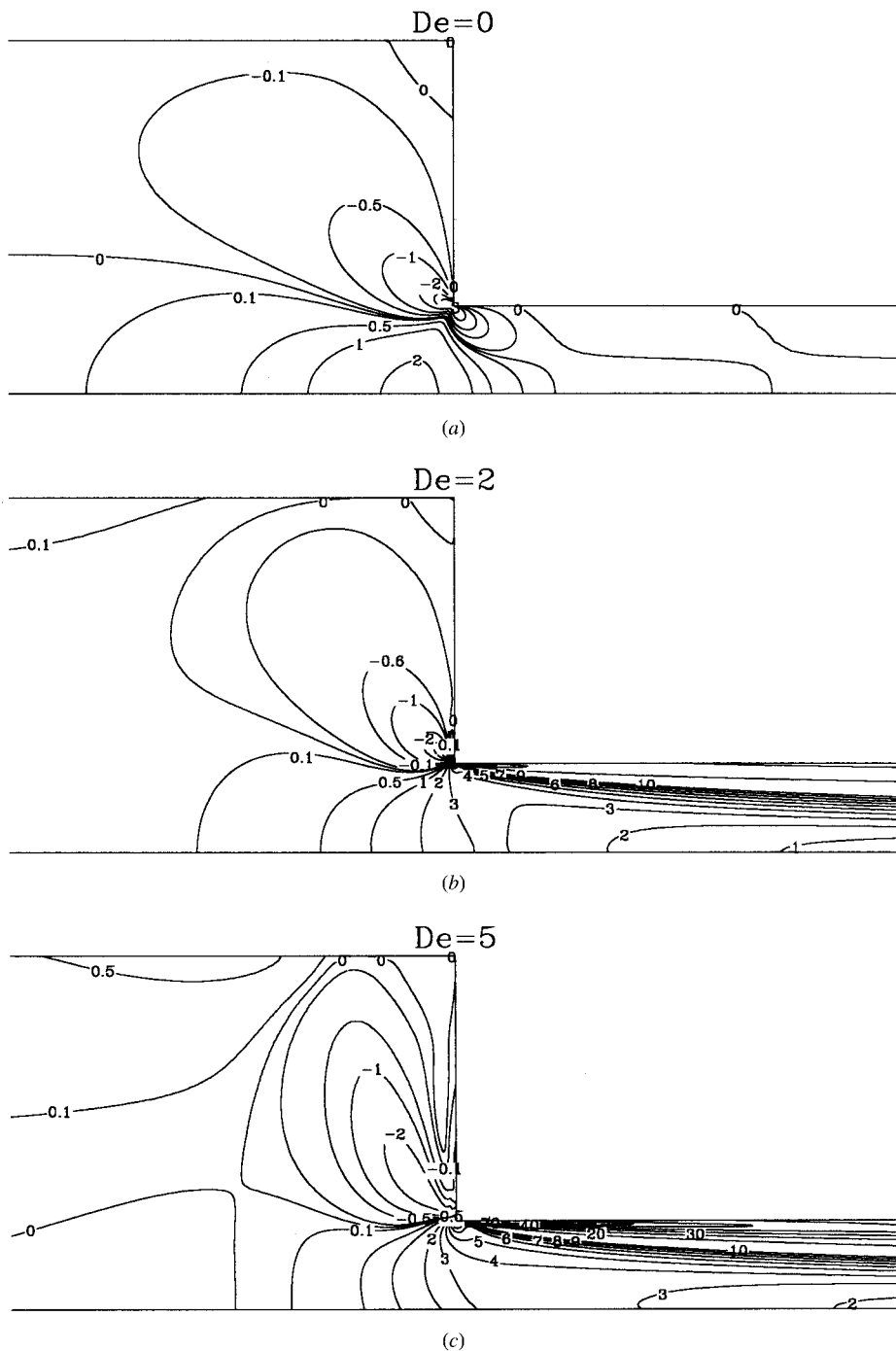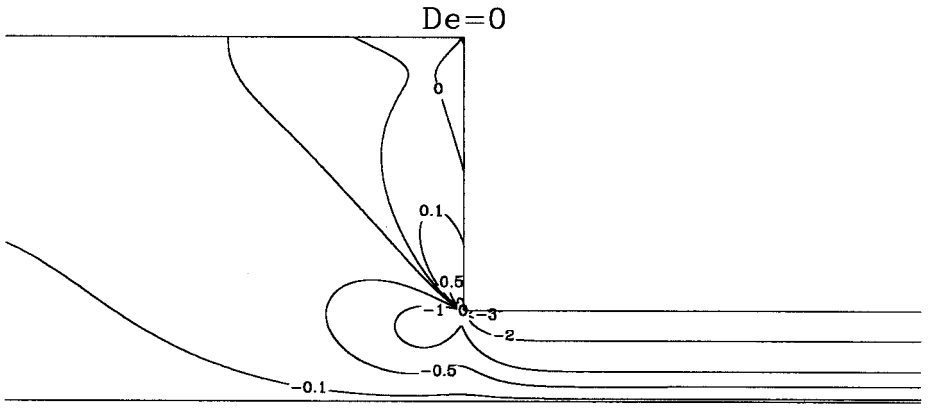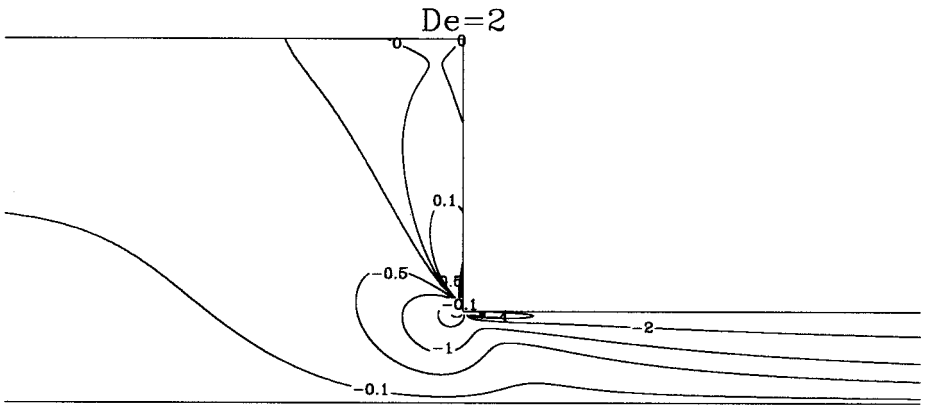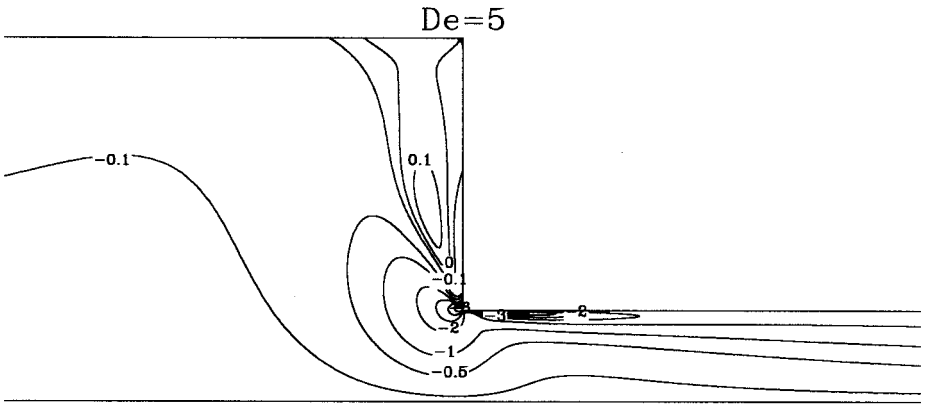
Figure 7. Contour maps of the nondimensional primary normal stress difference, N_1: (*a*) De = 0; (*b*) De = 2; (*c*) De = 5.

Figure 8. Contour maps of the nondimensional shear stress, T_{xy}: (*a*) De = 0; (*b*) De = 2; (*c*) De = 5.

(in round contractions) [20]. The sketches of vortex growth mechanisms given by Boger et al. [21] (see their Fig. 10), based on visualizations of viscoelastic entry flows, are closely emulated by the succession of streamline patterns in Figure 6.

Lip vortices, corner vortex enhancement, and the other differences between Newtonian and viscoelastic flow patterns seen in Figure 6 results from distinct stress structure, as can be inferred from Figures 7 and 8. The main differences are the very high normal and shear stresses that build up around the reentrant corner for viscoelastic fluids, and the enhancement of the elongational flow along the centerline evident in Figure 9, and caused by a large and positive N_1 at the entrance to the contraction. The stress field forces the viscoelastic fluid to be more deflected toward the centerline than the Newtonian or the less elastic fluids, where the flow is further accelerated by the positive T_{xx} gradients; as a consequence the axial velocity profiles of the viscoelastic fluid at the contraction plane are more uniform, and the centerline velocity reaches higher values than those of the Newtonian case and may even go beyond the fully developed value in the downstream channel, as shown in Figure 9. The centerline velocity overshoot effect has been observed in other simulations (cf. [6, 12]) and also experimentally (e.g., [22]), and the increase relative to its fully developed value is in reasonable agreement with other works where different fluids have been used (here we obtain 2.8%, 7.1%, and 17.8% for De = 1, 2, and 5, respectively; Xue et al. [12] got 4% for De = 1.6; Marchal and Crochet [6] got 22% for De = 4.7).

We end this work with a comparison between the new formulation used to obtain stresses at cell faces given by Eq. (15) and that proposed in a previous work [5]. The main difference between the two formulations lies on the way interpolation is done, which affects the results when nonuniform meshes are utilized. In the former formulation the forces acting on a surface across cell centers were interpolated directly (with arithmetic averaging) to the cell faces, thus the b_{li} were given by $\overline{B_l \tau_{ij} n_j}$ [cf. Eq. (16)]; however, it seems more correct to interpolate the stress components and then obtain forces at cell faces via the usual tensorial relationship, $\overline{T_i} = B_l \overline{\tau_{ij}} n_j$ (where B_l and n_i are now evaluated directly at cell faces, i.e., B_l is the scalar area of the cell face along direction l and n_i is its unit normal vector), as
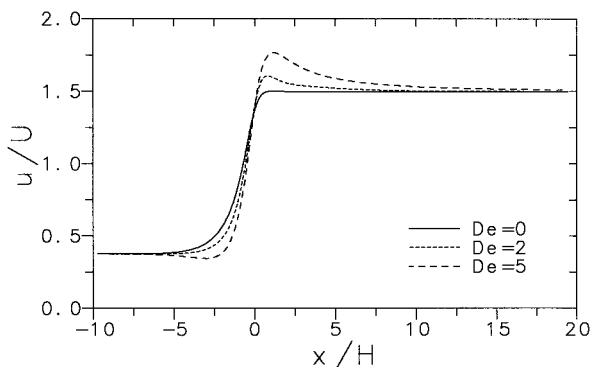

Figure 9. Variation of the longitudinal velocity component along the centerline for various Deborah number flows.

implied in the new formulation. Care should also be taken so that, in the limiting case of a uniform velocity field in a nonuniform mesh, the resulting cell-face stresses do vanish, and Eqs. (15)–(16) respect this premise. Figure 10 shows two transverse profiles of the longitudinal velocity component across the large channel, at $1H$ and $2H$ upstream of the contraction plane; some localized oscillations are visible at $y/H \approx 0.5H$, where an interface between two subblocks used to generate the mesh creates a sudden nonuniform mesh-spacing change. With the present formulation there are no oscillations, an indication of the better interpolation strategy achieved with Eq. (15).

5. CONCLUSIONS

A sequential segregated approach based on a general finite-volume methodology in nonstaggered meshes is shown to be effective in solving the flow motion equations in conjunction with arbitrary additional constitutive equations expressing stress-strain relationships. The test case chosen was the typical benchmark flow through an abrupt 4:1 planar contraction for Newtonian and viscoelastic fluids obeying the upper-convected Maxwell model. A new formulation to obtain stresses at cell faces shows improvement for nonuniform meshes, and inclusion of the div u term in the constitutive equation improves the stability and the convergence rate of the method.

Results are presented for a range of Deborah numbers from 0 to 8, and for Reynolds numbers of 0.5 and 1.0. The streamline patterns show the existence of corner and lip vortices at De $\simeq$ 1 to 4, and a vortex enhancement mechanism through lip vortex intensification followed by fingering of the corner vortex toward the lip, with subsequent enveloping and merging of the two, in agreement with the literature.

For the Newtonian model the results are identical to those obtained with a standard and well-validated code, and the computing time is just about 18% higher. For the UCM model the required computing time (and number of time steps)
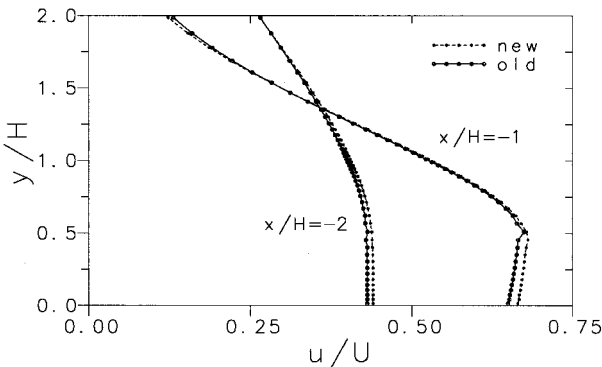

Figure 10. Influence of the cell-face stress formulation on the solution smoothness. Transverse profiles of the streamwise velocity in the upstream channel at $x/H = -2$ and -1, for De $= 5$.

tends to increase with the elasticity of the fluid. This was expected from the segregated nature of the method, with the stresses obtained from the constitutive equation being explicitly inserted into the momentum equations, and similar deterioration of the convergence rate is found in most methods reported in the literature. However, the present method shows good robustness, with solutions for the viscoelastic cases achieved for higher De numbers than with other existing methods and where, furthermore, the time step utilized in the computations was chosen based on the Newtonian case and was kept at a constant level for all runs.

REFERENCES

1. S. V. Patankar, *Numerical Heat Transfer and Fluid Flow*, Hemisphere, Washington, DC, 1980.
2. M. Perić, A Finite-Volume Method for the Prediction of Three-Dimensional Fluid Flow in Complex Ducts, Ph.D. thesis, Imperial College, University of London, 1985.
3. J. H. Ferziger and M. Perić, *Computational Methods for Fluid Dynamics*, Springer Verlag, Berlin, 1996.
4. C. M. Rhie and W. L. Chow, A Numerical Study of the Turbulent Flow Past an Airfoil with Trailing Edge Separation, *AIAA J.*, vol. 21, pp. 1525–1532, 1983.
5. P. J. Oliveira, F. T. Pinho, and G. A. Pinto, Numerical Simulation of Non-linear Elastic Flows with a General Collocated Finite-Volume Method, *J. Non-Newtonian Fluid Mech.*, vol. 78, pp. 1–43, 1998.
6. J. M. Marchal and M. J. Crochet, A New Mixed Finite Element Method for Calculating Viscoelastic Flow, *J. Non-Newtonian Fluid Mech.*, vol. 26, pp. 77–114, 1987.
7. J. Y. Yoo and Y. Na, A Numerical Study of the Planar Contraction Flow of a Viscoelastic Fluid Using the SIMPLER method, *J. Non-Newtonian Fluid Mech.*, vol. 29, pp. 89–106, 1991.
8. E. O. A. Carew, P. Townsend, and M. F. Webster, A Taylor-Petrov-Galerkin Algorithm for Viscoelastic Flow, *J. Non-Newtonian Fluid Mech.*, vol. 50, pp. 253–287, 1993.
9. T. Sato and S. M. Richardson, Explicit Numerical Simulation of Time-Dependent Viscoelastic Flow Problems by a Finite Element/Finite Volume Method, *J. Non-Newtonian Fluid Mech.*, vol. 51, pp. 249–275, 1994.
10. A. Baloch, P. Townsend, and M. F. Webster, On Vortex Development in Viscoelastic Expansion and Contraction Flows, *J. Non-Newtonian Fluid Mech.*, vol. 65, pp. 133–149, 1996.
11. H. Matallah, P. Townsend, and M. F. Webster, Recovery and Stress-Splitting Schemes for Viscoelastic Flows, *J. Non-Newtonian Fluid Mech.*, vol. 75, pp. 139–166, 1998.
12. S.-C. Xue, N. Phan-Thien, and R. I. Tanner, Three Dimensional Numerical Simulations of Viscoelastic Flows through Planar Contractions, *J. Non-Newtonian Fluid Mech.*, vol. 74, pp. 195–245, 1998.
13. R. B. Bird, R. Armstrong, and O. Hassager, *Dynamics of Polymeric Liquids, Vol. 1, Fluid Mechanics*, 2d ed., Wiley, New York, 1987.
14. R. B. Bird, C. F. Curtiss, R. C. Armstrong, and O. Hassager, *Dynamics of Polymeric Liquids, Vol. 2, Kinetic Theory*, 2d ed., Wiley, New York, 1987.
15. R. I. Issa and P. J. Oliveira, Numerical Predictions of Phase Separation in Two-Phase Flow through T-Junctions, *Comput. Fluids*, vol. 23, pp. 347–372, 1994.
16. P. J. Oliveira, Computer Modelling of Multidimensional Multiphase Flow and Application to T-Junctions, Ph.D. thesis, Imperial College, University of London, 1992.
17. J. P. Van Doormaal and G. D. Raithby, Enhancements of the SIMPLE Method for Predicting Incompressible Fluid Flows, *Numer. Heat Transfer*, vol. 7, pp. 147–163, 1984.

18. P. J. Oliveira and F. T. Pinho, Pressure Drop Coefficient of Laminar Newtonian Flow in Axisymmetric Sudden Expansions, *Int. J. Heat Fluid Flow*, vol. 18, pp. 518−529, 1997.

19. F. Ferziger and M. Perić, Further Discussion of Numerical Errors in CFD, *Int. J. Numer. Meth. Eng.*, vol. 23, pp. 1263−1274, 1996.

20. D. V. Boger and K. Walters, *Rheological Phenomena in Focus*, Rheology Series, Vol. 4, Elsevier, Amsterdam, 1993.

21. D. V. Boger, D. U. Hur, and R. J. Binnington, Further Observations of Elastic Effects in Tubular Entry Flows, *J. Non-Newtonian Fluid Mech.*, vol. 20, pp. 31−49, 1986.

22. L. Quinzani, R. C. Armstrong, and R. A. Brown, Birefringence and Laser-Doppler Velocimetry (LDV) Studies of Viscoelastic Flow through a Planar Contraction, *J. Non-Newtonian Fluid Mech.*, vol. 52, pp. 1−36, 1994.